Investigation on the Electrothermal Performance of a High Temperature Superconducting Cable in an Offshore Wind Farm Integrated Power System: Fault and Islanding Conditions

Alireza Sadeghi, Seyyedmeysam Seyyedbarzegar, and Mohammad Yazdani-Asrami, *Member, IEEE*

***Abstract*-- The main contribution of this paper is to study the electrothermal performance of a 22.9 kV High Temperature Superconducting (HTS) AC cable under transients such as short circuit faults and Islanding Operating Mode (IOM) of a wind farm. For this purpose, an HTS cable connects a 12 MVA doubly-fed induction generator-based wind farm to the load centre, under two different scenarios of the network. In the first scenario, the upstream grid is located far away from the load centre and most of the demanded load is supplied by the wind farm while in the second scenario, part of the load is supplied by the wind farm and the rest is supplied by the upstream grid located near the load centre. In case of faults and transients in upstream grid, protection systems isolate the wind farm and thus it operates in a specific mode, called as IOM. Results indicated that the location of faults and transients especially IOMs play a significant role in the electrothermal performance of HTS cable.**

***Index Terms*-- HTS cable, Islanding operation mode, Resistance, Temperature, Offshore wind farm, Wind power**

I. Introduction

To avoid the consequences of the global warming caused by greenhouse gases, the Kyoto Protocol and the Paris agreement proposed the efficiency enhancements of the power systems as well as application and integration of more Renewable Energy Resources (RESs) [1]. Among all available RESs, offshore wind farms are the most promising energy resources that use wind turbines (WT) to convert the mechanical power of the wind into the electrical energy [2]. High Temperature Superconducting (HTS) cables were proposed as candidates to deliver the generated electrical energy to the shore with much lower loss, extremely higher current carrying capacity, and lower voltage level compared to conventional power cables [3]. Superconductivity is investigated to be used in many power systems and

Manuscript received March 21, 2022, revised July 20, 2022, accepted August 03, 2022. (Corresponding author's email: m.yazdaniasrami@gmail.com, mohammad.yazdani-asrami@glasgow.ac.uk)

A. Sadeghi and S. M Seyyedbarzegar are with Department of Electrical Engineering, Shahrood University of Technology, Shahrood, Iran.

M. Yazdani-Asrami is with Propulsion, Electrification, & Superconductivity group, Autonomous Systems & Connectivity division, James Watt School of Engineering, University of Glasgow, Glasgow, G12 8QQ, United Kingdom.

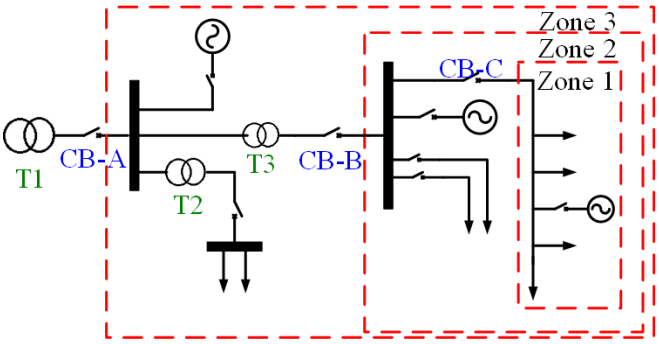

Figure 1. The structure of the grid that could operate in Islanding Operating Mode, with respect to different (triple) protection zones, CB stands for Circuit Breaker and T stands for transformer

Cryo-electrified transportation applications [4], [5], such as HTS transformers [6], [7], superconducting fault current limiters [8]–[10], superconducting rotational machines [11], [12], and HTS cables [13]–[15]. Although the integration of HTS cables into power systems with wind farms was investigated in the literature, most of the related papers have focused on investigating the steady-state characteristic of HTS cables, affected by the presence of wind farms [16]–[18]. Also an investigation on the fault performance of DC HTS cables in presence of wind farms has been discussed in [19], however; this reference concentrated more on the modelling procedure of the grid side and rotor side converter units rather than evaluating the impact of different grid transients on the fault characteristic of HTS cable. Under faults and transients, the HTS cables may suffer a rapid and massive temperature rise that could lead to deformation, delamination and burnout of superconducting tapes, and many other consequences. On the other hand, in presence of wind farms, the fault current level is increased and this needs to be considered while designing or fabricating an HTS cable as it may increases the possibility of burnouts and deformations. Based on different types of short circuit faults of power systems, they can be studied in different regions of the power system. Besides the usual short circuit faults, there are other transient conditions that could impose challenges to the appropriate performance of the power system. Islanding Operating Mode (IOM) is one

of these transients. IOM is defined as a term that describes a state of the Distributed Generation (DG) units with part of the power system connected to the load. As shown in Fig. 1, when part of the network including DG unit and electric loads are operating independently from the main power system, the isolated area is placed in an electrical islanded area. Based on this, the term of IOM refers to the principles that the operation of the desired area is independent from the parameters of the main grid and its energization is done through DG units [20]. The islanded region might be consisted of several zones and different voltage levels. It is also possible that each zone is connected to one or more disconnection points. In general, the different islanded zones are the consequence of different operation of Circuit Breakers (CBs). Three possible zones for islanding and disconnection points can be seen in Fig. 1. On the other hand, islanding of the power grid can occur due to faults or malfunctions of the upstream power system that is known as unintentional IOM. Aforementioned malfunctions entail many temporary and permanent risks that can ultimately affect the stability of the islanded area [21]. Also unintentional IOMs could result in reduction of power quality, voltage and frequency collapse, loss of grounding, load shedding, over-frequency fluctuation of DG units, DG units tripping, etc. [22]. One of the most important factors that threaten the stability of the islanded area is the imbalance between load and generated electrical power by DG units. In general, the imbalance between load and generation will lead to the creation of severe transient states that will damage the equipment in islanded area. Meanwhile, the balance between load and generation will lead to a high level of stability in the electrically islanded region with a neglectable transient period that applies the least stress to the power devices. Under these conditions, DG units in the islanded region will be able to supply the required load [23], [24]. Therefore, fault and transient performance evaluation of HTS cables in wind farms plays a key role for supplying the load without any interruptions and blackouts that is discussed in this paper in detail.

In this paper, performance of a triaxial 22.9 kV AC HTS cable connected to a 12 MVA Doubly-Fed Induction Generator (DFIG)-based wind farm is investigated under transients. An Equivalent Circuit Model (ECM) is used to characterise the electrothermal behaviour of the HTS cable. The geometrical structure of the understudied cable and its main specifications are shown in Fig. 2 and Table 1, respectively [25]. In this cable, for achieving a balanced current distribution, phase A consists of two superconducting layers and phase B has also two formers for guaranteeing a higher mechanical withstanding against massive fault currents [26], [27]. An attempt has been made to examine the performance of the power grid in islanding operating mode, along with the faults that occurred in different parts of the grid. In this regard, based on different arrangements of the network and the balance/imbalance between load and generation in the islanded area, two scenarios were defined and the performance of the superconducting cable was investigated.

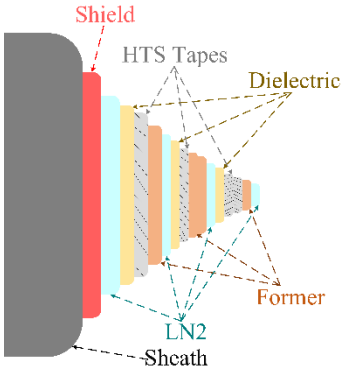

Figure 2. The structure of the understudied cold-dielectric AC HTS cable

Table 1. Specifications of the understudied HTS cable

Item	Value or Type	Unit
Tape	YBCO	-
Operating Temperature	70	K
Shield Layer	Copper	-
Insulation Layer	PPLP	-
Former Radii [A B1 B2 C]	[17 20 21 28]	mm
Cryogenic Coolant	LN2	-
Shield Layer Thickness	1	mm
Critical Temperature of tape	92	K
Critical Current of HTS tapes	150	A
Critical Current of Cable	4.2	kA

II. Equivalent Circuit Modelling: DFIG in Wind Turbine and HTS Cable

A. DFIG in Wind Turbine

Fig. 3 illustrates the ECM of the DFIG used as the main power conversion units in the wind turbines. Equations (1) to (4) express the voltage of stator and rotor in $dq0$ reference frame [28]:

$$v_{ds} = r_s i_{ds} + \omega_s \psi_{qs} \quad (1)$$

$$v_{qs} = r_s i_{qs} - \omega_s \psi_{ds} \quad (2)$$

$$v_{dr} = r_r i_{dr} - s\omega_s \psi_{qr} + \frac{d\psi_{dr}}{dt} \quad (3)$$

$$v_{qr} = r_r i_{qr} + s\omega_s \psi_{dr} + \frac{d\psi_{qr}}{dt} \quad (4)$$

where, v_{ds} and v_{qs} are the stator voltages in d and q reference frame, respectively; i_{ds} and i_{qs} are the stator currents in d and q reference frame, respectively, ω_s is the synchronous angular frequency, ψ_{qs} and ψ_{ds} are flux linkage of the stator in d and q reference frame, respectively, s is rotor slip, and r_s is stator resistance. Also v_{dr} and v_{qr} are the rotor voltages in d and q

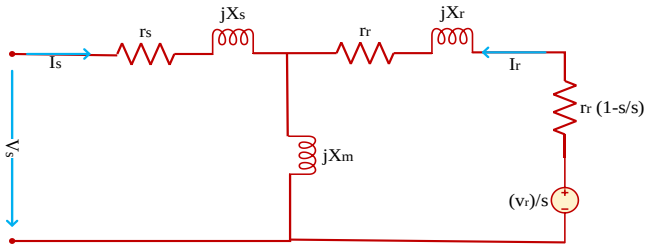

Figure 3. ECM of the DFIG-based wind turbine

reference frame, respectively; the same is also valid for current, resistance, and the flux linkage of the rotor with the subscript of (r).

The flux linkages of the rotor and the stator in the $dq0$ reference frame are modelled through equations (5) to (8), where L_{ss} is stator inductance, L_{rr} is rotor inductance, and L_m is mutual inductance between rotor and stator [28].

$$\psi_{ds} = -L_{ss} i_{ds} + L_m i_{dr} \quad (5)$$

$$\psi_{qs} = -L_{ss} i_{qs} + L_m i_{qr} \quad (6)$$

$$\psi_{dr} = -L_m i_{ds} + L_{rr} i_{dr} \quad (7)$$

$$\psi_{qr} = -L_m i_{qs} + L_{rr} i_{qr} \quad (8)$$

Electromagnetic torque generated by DFIG is modelled by using equation (9) [28]:

$$T_{em} = \psi_{qr} i_{dr} - \psi_{dr} i_{qr} \quad (9)$$

For the fault analysis of the DFIG, the following equations are used. Equations (10) to (14) express the voltage of stator and rotor in transient mode, where E'_d and E'_q are the voltage induced in X'as the transient reactance of the DFIG [28].

$$v_{ds} = r_s i_{ds} - X' i_{qs} + E'_d \quad (10)$$

$$v_{qs} = r_s i_{qs} - X' i_{ds} + E'_q \quad (11)$$

$$E'_d = \frac{\omega_s L_m \varphi_{qr}}{L_{rr}} \quad (12)$$

$$E'_q = \frac{-\omega_s L_m \varphi_{dr}}{L_{rr}} \quad (13)$$

$$X' = \omega_s \left(\frac{L_{ss} - L_m^2}{L_{rr}} \right) \quad (14)$$

In the transient state of the grid, the electromagnetic torque of the wind turbine is modelled using equation (15) [28]:

$$T_{em} = v_{ds} i_{ds} + v_{qs} i_{qs} - r_s \left(i_{ds}^2 + i_{qs}^2 \right) \quad (15)$$

In equation (15), it is assumed that the synchronous velocity is equal to 1 per unit and the electromagnetic torque is in per unit [28].

The active and reactive powers generated by DFIG-based wind turbine are modelled using equations (16) to (19) [28]:

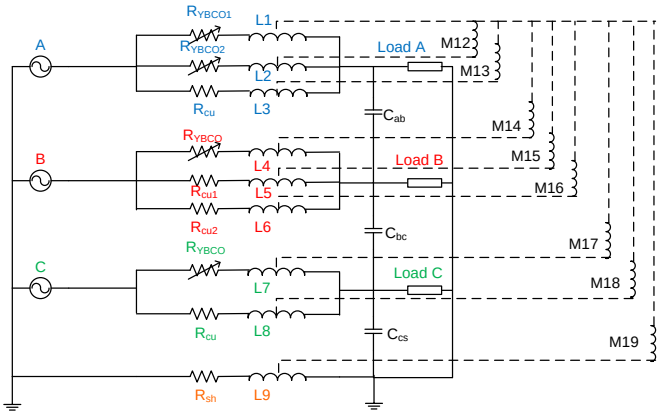

Figure 4. ECM of the understudied HTS cable (To avoid drawing complications, only mutual-inductances with respect to the first superconducting layer of phase A are shown here, however all must be considered in simulations.)

$$P_s = v_{ds} i_{ds} + v_{qs} i_{qs} \quad (16)$$

$$Q_s = v_{qs} i_{ds} - v_{ds} i_{qs} \quad (17)$$

$$P_r = v_{dr} i_{dr} + v_{qr} i_{qr} \quad (18)$$

$$Q_r = v_{qr} i_{dr} - v_{dr} i_{qr} \quad (19)$$

The control loops for the grid-side and the rotor-side converters and the wind turbine are discussed in detail in [29].

B. HTS Cable

Fig. 4 is presented as ECM of understudied cable that consists of different electric circuit elements including variable resistances (varistors), constant resistances, self and mutual-inductances, and capacitances. Varistors model the resistivity of HTS layer in superconducting tapes, while constant resistances model the resistivity of formers and shield layers of the cable. Inductances are used to model the electromagnetic interdependency of different layers and phases while the impact of insulations and dielectrics are modelled through the capacitances. It should be also mentioned that to avoid complications in figure drawing and illustration, only mutual-inductances with respect to the first superconducting layer of phase A are shown in Fig. 4, however; all of these circuit element were considered and implemented in simulations.

The resistivity of YBCO layer can be calculated based on equations (20) to (22) for all different operating modes of the cable [27].

$$\rho_{t2} = \rho_{t1} + \left(\frac{E_0}{J} \right) \left(\frac{J}{J_c(T)} - 1 \right)^{n(T,B)} \quad if \quad J_c(T,B) < J < 3\,J_c(T,B) \quad (20)$$

$$\frac{1}{\rho_{t3}} = \frac{\rho_{t2} + \rho_{sat}}{\rho_{t2} \cdot \rho_{sat}} \quad if \quad J > 3\,J_c(T,B) \quad (21)$$

$$\rho_i = \rho_{i-1}[1 + h_c(T_i - T_{i-1})] \quad (22)$$

where, ρ_{ti} is the resistivity of tapes in each operational state, J_c is the critical current density of tapes, E_0 is 0.1 V/cm, J is transport current density, T_i is the temperature in ith step time, $n(T,B)$ is the temperature and field dependant index value of YBCO tapes, h_c is considered to be 10^{-4}, which is the temperature dependence coefficient of YBCO resistivity in

normal metal state, and ρ_{sat} is assumed to be 90 μΩcm. The ρ_{sat} models the highly resistive nature of superconducting material after transition into non-superconducting state. Under such circumstances, the resistivity of YBCO layer increases slightly with respect to temperature and no more with respect to current that is characterised as a saturated resistance [30], [31].

In the transient state such as a short circuit fault, the current surpasses the critical current and this results in an abrupt temperature rise until the superconducting tapes transit to the normal metal region. As a consequence, the resistivity of the HTS tapes increases dramatically, and fault current passes through the former. The induced heat load per unit length due to this transition, and the temperature transient under adiabatic assumption, can be calculated according to equations (23) and (24) [30]:

$$DC_P(T)\frac{dT}{dt} = G(T, I_f) \tag{23}$$

$$G(T,I) = \begin{cases} \dfrac{\rho_{tape}(T) I_{tape}\left(I_{tape} - I_c(T,B)\right)}{S_{ybco}} & T < T_c \\ \rho_{former}(T)\left(\dfrac{I_{former}^2}{S_{former}}\right) & T \geq T_c \end{cases} \tag{24}$$

where D is the density of YBCO, $C_P(T)$ is the temperature dependant specific heat capacity, $G(T, I_f)$ is the generated heat load due to the fault current I_f at temperature T through the former/YBCO, $\rho_{tape}(T)$ refers to temperature-dependent resistivity of YBCO layer, I_{tape} is the part of the fault current passes through HTS tapes, $I_c(T, B)$ is the degraded critical current with respect to temperature, field, and strain, S_{tape} refers to the cross-section of HTS tapes, $\rho_{former}(T)$ temperature-dependent resistivity of the copper former, I_{former} is the part of the fault current passes through former, and S_{former} refers to the cross-section of the former [30].

At last, equations (25) and (26) represent the thermal behaviour of the HTS cable when the cable is recovering from a fault [30], [32]:

$$DC_P(T)\frac{dT}{dt} = G(T,I) - Q(T,I) \tag{25}$$

$$Q(T,I) = \frac{k_{LN2}(T)\left(T - T_{op}\right) \times P_h}{D_e} \tag{26}$$

where, $Q(T,I)$ is heat transfer term, $k_{LN2}(T)$ is thermal conductivity of coolant fluid at temperature T, P_h is the hydraulic area, and D_e is the effective diameter of the cryostat. It should be noted that the expressed heat transfer equation during heating phase of the cable, equation (20), took place in complete adiabatic conditions. This is due to the presence of a thick insulation with a low value of thermal conductivity. On the other hand, in equation (25), the heat transfer is not in a complete adiabatic balance and convective heat transfer causes the temperature reduction of HTS cable, during cooling phase.

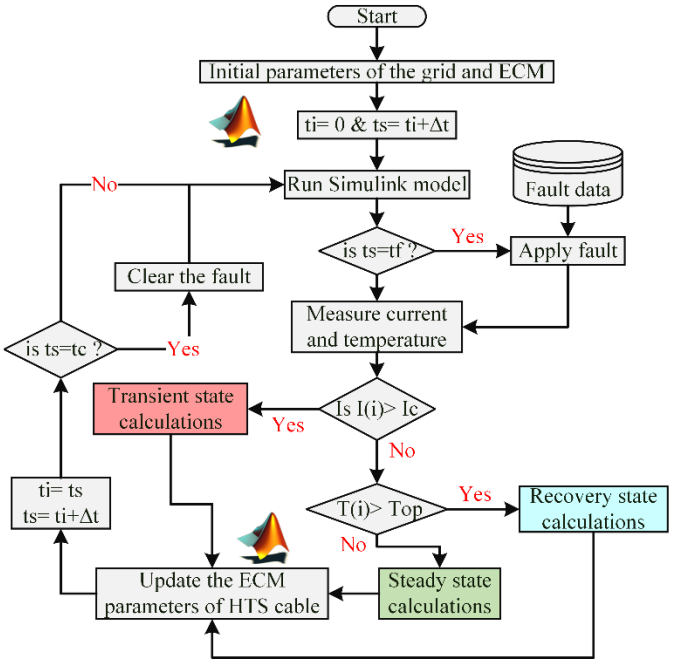

Figure 5. The modelling procedure flowchart of understudied HTS cable for different operating conditions, i.e. steady state, transient, and recovery

The flowchart for modelling procedure of the HTS cable is shown in Fig. 5 [30]. So, according to the values of current and temperature in each time step, the model can decide which formulations must be applied for the electrothermal characteristic of the HTS cable [30].

III. Results and Discussions

According to Fig. 6, the grid is consisted of three main areas, namely the upstream grid, load centre, and the wind farm region that includes HTS cable. The upstream grid is connected to the load centre through a 230 kV Overhead Transmission Line (OHTL) and modelled as an infinite bus. The wind farm area supplies part/all of the demanded electricity of the load through a 22.9 kV AC HTS cable. Table 2 tabulates some parameters of the test grid. As shown in Fig. 6, two scenarios for the structure of the grid are considered. In the first scenario, the load centre is far from the upstream grid and it demands approximately the same power as the output power of the wind farm. Under such circumstances, the load is 10 MVA and the OHTL has a length of 50 km. This grid scenario would be referred to as "*S1*" in the rest of the paper. In the second scenario, the load centre demands a power way higher than the maximum generated power of the wind farm. As a result, part of the load must be supplied by the upstream grid. To analyse this scenario, the load is considered to be 50 MVA and the length of OHTL is 5 km. This scenario would be referred to as "*S2*". The rationale behind the selection of these two scenarios is that in both cases all generated power of

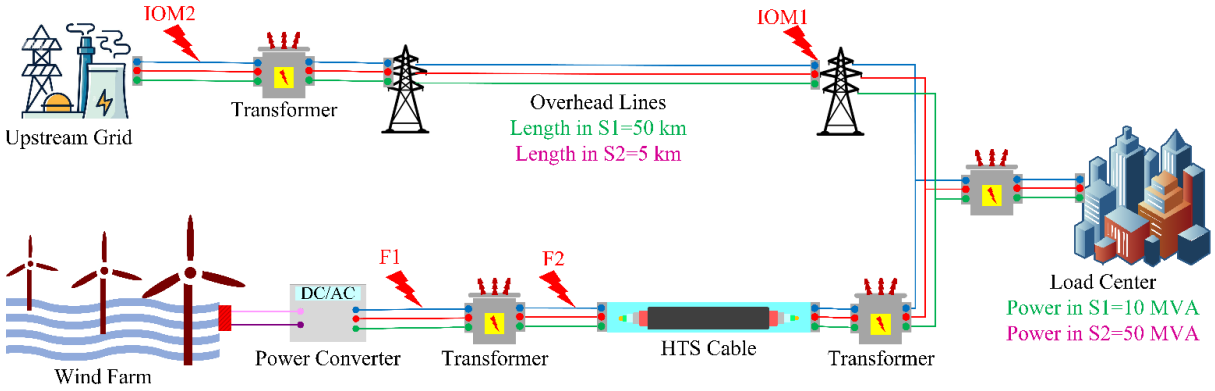

Figure 6. The configuration of the test grid for characterising the transient behaviour of HTS cable when connected to an offshore wind farm

Table 2. Grid parameters used in modelling process, under different scenarios of the test grid

Parameter	Value	Unit	Description
V_g	63	kV	Grid voltage
V_{tohl}	230	kV	OHTL voltage
V_{load}	20	kV	Load voltage
V_{hts}	22.9	kV	HTS cable voltage
$V_{o\text{-}wind}$	575	V	Output voltage of wind turbines
S_{load}	50	MVA	Apparent power of load
$S_{o\text{-}wind}$	1.5	MVA	Output power of each wind turbine
f	50	Hz	Frequency
n	8	*	Number of turbines in a wind farm
L_{tohl}	50 & 5	km	Length of transmission overhead line
L_{hts}	3	km	Length of HTS cable
S_{load}	10 & 50	MVA	Apparent power of load
$[R_1\ R_0]$	[0.01273 0.3864]	Ohms/km	Positive- and zero-sequence resistances of OHTL
$[L_1\ L_0]$	[0.9337 4.1264]	mH/km	Positive- and zero-sequence inductances of OHTL
$[C_1\ C_0]$	[12.74 7.75]	nF/km	Positive- and zero-sequence capacitances of OHTL
C_{HTS}	60	nF	Capacitance of HTS cable
L_{HTS}	2.3	μH	Inductance of HTS cable

wind farm is consumed by the load. This means that in neither of these scenarios, the wind farm is served as a backup generation unit and in both of them the HTS cable always operates at full load. These two configurations are adapted based on the grids presented in [33], [34]. The structure of the wind turbine is depicted in Fig. 7 and its main parameters are listed in Table 3 [29]. In each scenario of the test grid structure, four fault scenarios were defined, as listed in Table 4 and located in Fig. 6. Different scenarios were chosen to cover different characteristics of the system and understudied HTS cable.

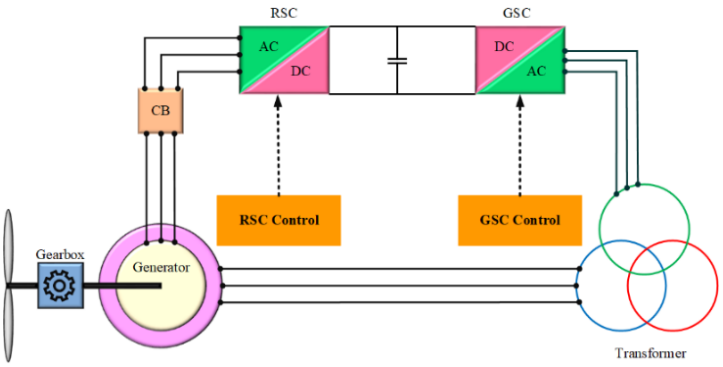

Figure 7. A simple diagram of DFIG-based wind turbine, RSC stands for rotor side converter, GSC stands for grid side converter, and CB stands for circuit breaker

Table 3. Parameters of wind turbine and its DFIG

Parameter	Value	Unit
Grid-side phase voltage	575	kV
DC capacitor	2000	μF
Grid side frequency	50	Hz
Rated wind speed	12	m/s

Table 4.Transient scenarios in different locations

Transient	Location
F1	Farm side- between transformer and farm (fault)
F2	Farm side- between transformer and HTS cable (fault)
IOM1	Upstream grid side- on OHL (IOM)
IOM2	Upstream grid side- between grid and transformer (IOM)

The impact of HTS cable presence on the fault current of the grid is shown in Fig. 8. As can be seen, the fault current is reduced (limited) in presence of HTS cable that is due to increasing the resistance of HTS tapes. This is a solid prove for using HTS cables integrated with wind farms could change the fault current level of the grid and protect the wind turbines. It should be mention that understudied cable has not been designed as a current limiting HTS cable, and if it was appropriately designed for such purpose, it could limit the fault much better.

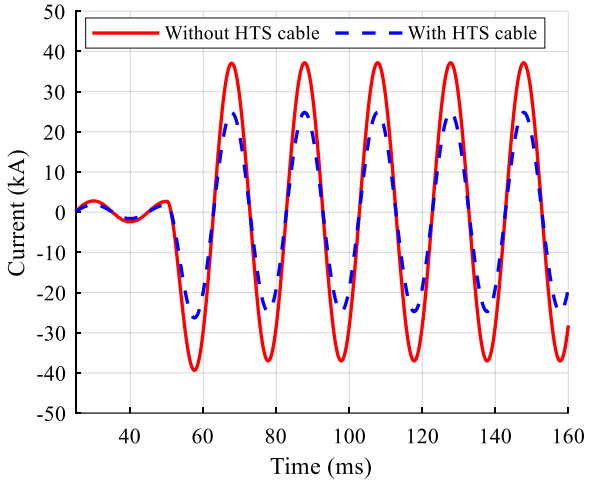

Figure 8. The impact of presence and absence of HTS cable on fault current in the test grid

A. The electrothermal analysis of HTS cable under fault

By applying F1 fault, a fault current is passing through the cable as shown in Fig. 9 under two S1 and S2 grid scenarios. The maximum fault current of S1 is increased by 7.7% in comparison to the fault current of S2. Thus, the temperature of the HTS tapes increases as shown in Fig. 10. According to this figure, the inner phase with a smaller former cross-section experiences a higher heat load. This can be justified with respect to the equation of generated heat in copper and Ohm's law which are $Q_{heat} = R_{cu} I_f^2 t$ and $R = \frac{\rho l}{A}$, respectively. The temperature difference in different layers of the understudied HTS cable initiates in different thermal mass of former layers with respect to their different radii. Under such circumstances, the outer layers have higher thermal mass and thus, a higher current or a longer fault/transient is required to increase their temperature. Therefore, in S1, the maximum temperature of the HTS cable in phase A after a 200 ms fault is 24.6% higher than phase B and 44.9% higher than phase C, as the outermost layer. By comparing the temperature of S1 and S2, it can be seen that the temperature of phase A in S1 is 1.1% higher than that of S2 while this number for phase B and C is 2.55% and 0.37%, respectively.

To compare two scenarios of the test grid, Table 5 lists the maximum fault current of each transient (fault or IOM) scenario in different phases. The significant difference between transient currents for each grid scenario is in case of the IOM1 and IOM2. In S1, after clearance of IMO1 and IOM2, a higher current than rated current imposes on the cable. While in S2 and for the same transient, an extremely massive current is passing through the system with a much higher frequency. High amplitude and frequency of such transient current is due to high level of unbalance between load and generation. This current under IOM2 for S1 and S2 are shown in Fig. 11(a) and Fig. 11(b), respectively which will be discussed in details in the following subsections.

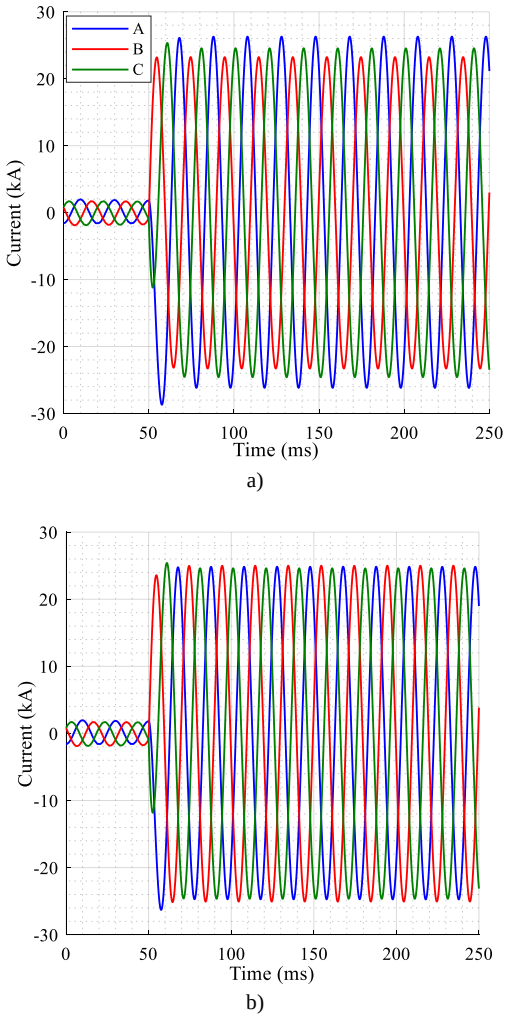

Figure 9. Fault current passing through the understudied HTS cable by F1 fault and under, a) S1 scenario, b) S2 scenario

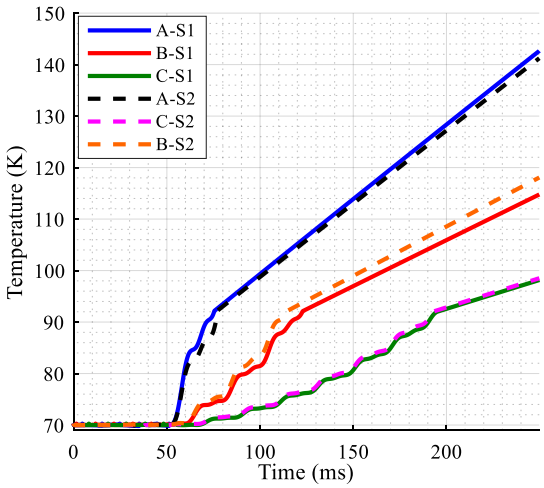

Figure 10. The temperature increase in the understudied HTS cable under F1 fault

Table 5. Maximum transient currents passing through HTS cable under different grid scenarios

Transient scenario	Phase	Transient Current of Grid (kA) under	
		S1	S2
F1	A	27.75	26.52
	B	23.23	26.01
	C	25.34	25.68
F2	A	76.39	79.08
	B	58.12	60.97
	C	59.55	60.92
IOM1	A	2.26	87.36
	B	2.18	85.14
	C	2.26	86.29
IOM2	A	2.58	89.53
	B	2.23	87.94
	C	2.36	88.11

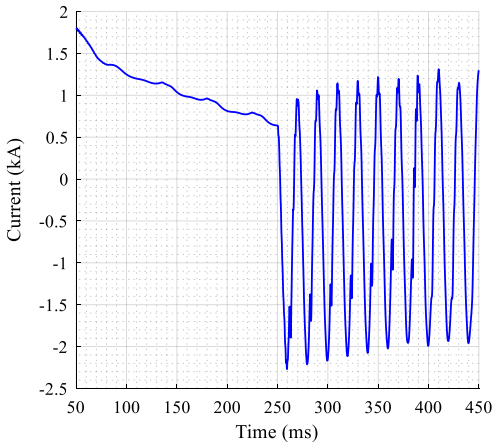

a)

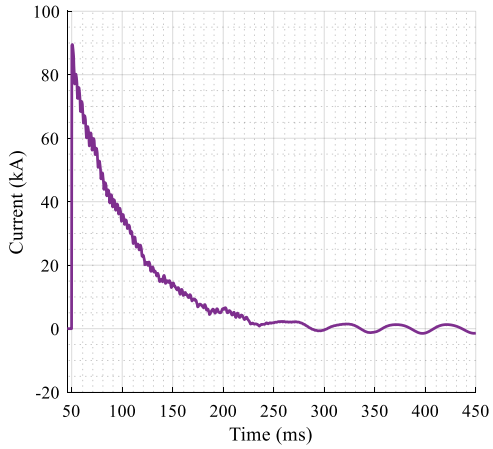

b)

Figure 11. Transient current of the understudied HTS cable under IOM2 transient scenario, a) for S1, b) for S2

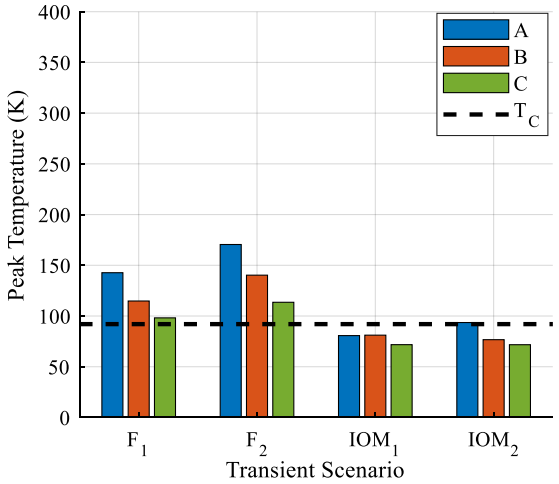

a)

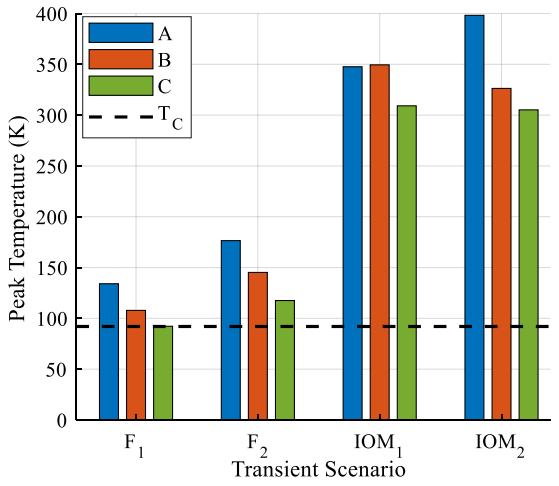

b)

Figure 12. Maximum temperature in different phases of the HTS cable under different transient scenarios for, a) S1, b) S2

Fig. 12 presents the maximum temperature of the HTS cable for different transient scenarios and different grid structures. As can be seen in this figure, under F1 and F2 faults and in both S1 and S2 structures of the grid, maximum temperature of the superconducting tapes surpasses the critical temperature (T_C) of the YBCO tapes and this results in the transition of HTS tapes into normal metal state. The main difference between the various grid structures lay in IOM1 and IOM2 transients. In S1, IOM1 and IOM2 are not capable of increasing the temperature of tapes beyond the T_C and this can lead to flux-flow state or very late transition and as a consequence, burn-out of tapes is probable. On the other hand, IOM1 and IOM2 transients, in S2 structure, cause a rapid and massive increase in the temperature of the HTS tapes and this could lead to thermal runaway of the tapes. Among these IOM scenarios, IOM2 imposes a higher transient current to the cable and can be assumed as worst-case scenario.

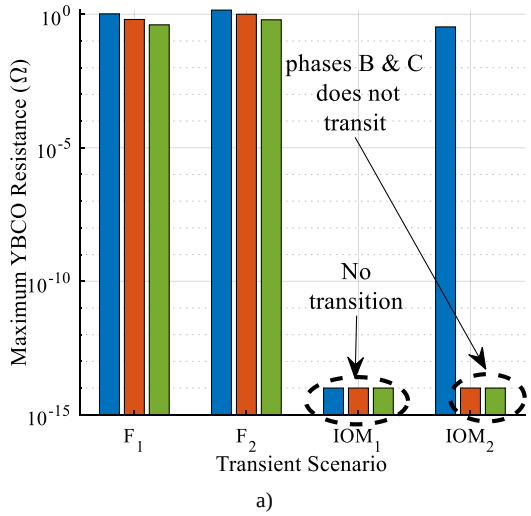

Figure 13. Maximum resistance in different phases of the understudied HTS cable under different transient scenarios for, a) S1, b) S2

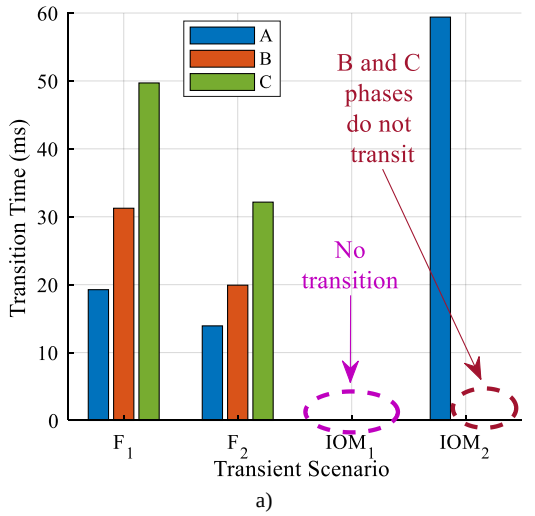

Figure 14. Transition time in different phases of the understudied HTS cable under different transient scenarios for, a) S1, b) S2

The electrical resistance of the superconducting tapes is illustrated in Fig. 13 with respect to the different transient scenarios. The resistance in phases which does not transit to the normal metal state in S1, are barely increased and become lower than the former layer or equal to it. As a consequence, part of the transient current passes through the HTS tapes, and by being in flux-flow mode, they could be damaged or burnt.

Transition time is another factor that is directly related to the temperature of the cable. The sharper temperature rises, faster the transition occurs. As shown in Fig. 14, the HTS tapes in phase C, for both S1 and S2 and in F1 and F2 scenarios, transit to the normal metal region slower than phase A and phase B. This is due to the fact that the temperature in this phase increases slower and less sharply than the B and A phases.

The maximum magnetic field induced in each phase of the cable is shown in Fig. 15. This figure can be interpreted with respect to the various twisting angles in each phase of the cable. This means that the higher value of twisting angle results in lower value of magnetic field, however; in understudied cable phase A consists of two HTS layers that are twisted in opposite directions. This results the magnetic field of phase A to be reduced. The outer phase (phase C) has a lower twisting angle in comparison to other phases and so has a lower magnetic field. However, due to opposite twisted HTS tapes in phase A, it has a lower magnetic field than phase B.

B. Impact of Wind speed

The performance of the wind turbine at wind speeds lower than the nominal speed is discussed here. During grid steady-state, variations of wind speed do not impose any challenge to the HTS cables while during a fault, wind speed can be harmful to them. According to Table 6, the variations of fault current with respect to the wind speed lead to different electrothermal behaviour. Since the fault current in the two grid scenarios is nearly the same as each other, the temperature and the resistance in each structure have a slight difference.

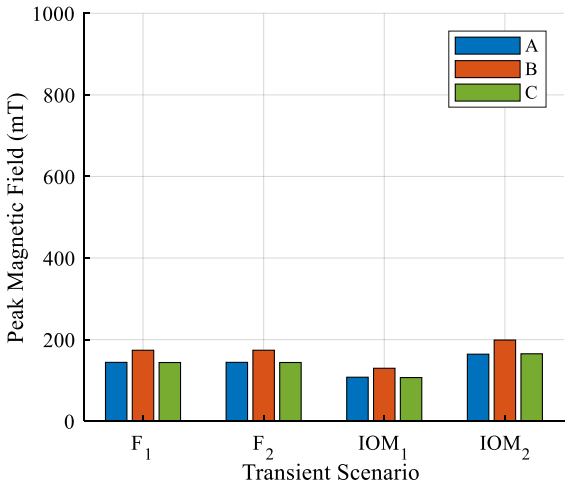

a)

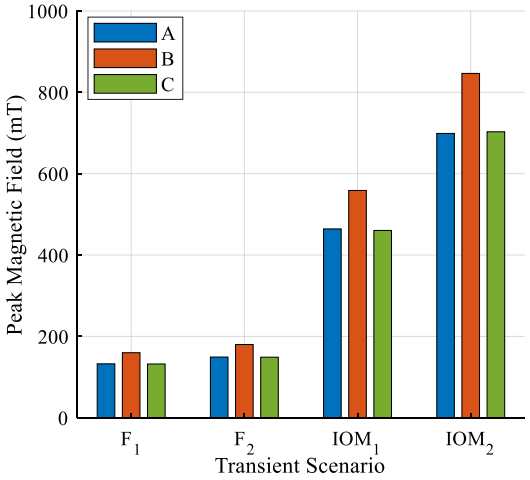

b)

Figure 15. Maximum magnetic field in different phases of the understudied HTS cable under different transient scenarios for, a) S1, b) S2

However, the difference in temperatures and resistances for wind speed variations between different grid scenarios is notable.

The values of the fault currents in each phase under different wind speeds are shown in Fig. 16 that are imposed on the grid as a consequence of F1 fault. The worst-case scenario is related to phase A with a 19.5 to 30 kA fault current under S1 and 18.5 to 28.5 kA under S2. For this phase, the maximum fault current increases by 35.9%, when the wind speed changes from 6 m/s to 10 m/s whilst, the maximum fault current increases by 13.2% for speeds between 10 m/s to 12 m/s. Clearly, these changes at the amplitude of the fault current result in different values of temperatures and resistances under each wind speed. As presented in Table 6, for 6 m/s wind speed, phase B hardly transits to normal state under S1. This is also valid for phase C and in both scenarios of the grid which result in the maximum temperature of 93 to 93.9 K.

Table 6. Electrothermal characteristic of the understudied HTS cable with respect to variations of wind speed for F1 fault

Parameter	Phase	Test grid structure	Wind Speed (m/s)			
			6	8	10	12
T (K)	A	S1	119.95	128.22	137.11	142.61
		S2	118.84	122.96	134.14	142.61
	B	S1	92.42	99.68	107.73	114.75
		S2	97.94	99.87	110.80	118.37
	C	S1	93.91	94.09	95.89	98.14
		S2	93.01	94.88	95.69	98.15
R (Ω)	A	S1	0.67	0.79	0.95	1
		S2	0.65	0.70	0.92	1.01
	B	S1	0.66	0.78	0.9	0.95
		S2	0.7	0.78	0.92	1
	C	S1	0.65	0.78	0.93	0.92
		S2	0.65	0.78	0.9	0.96

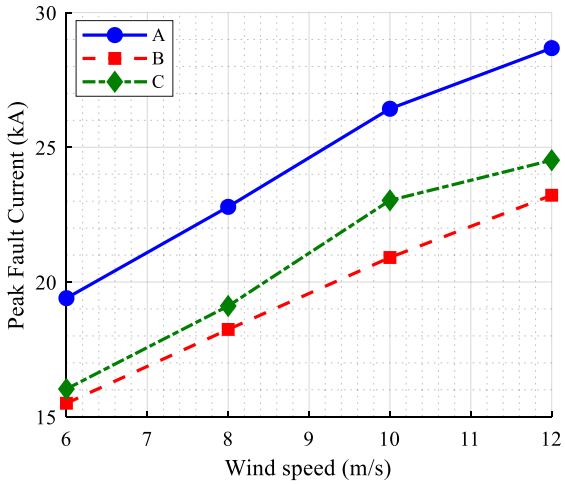

a)

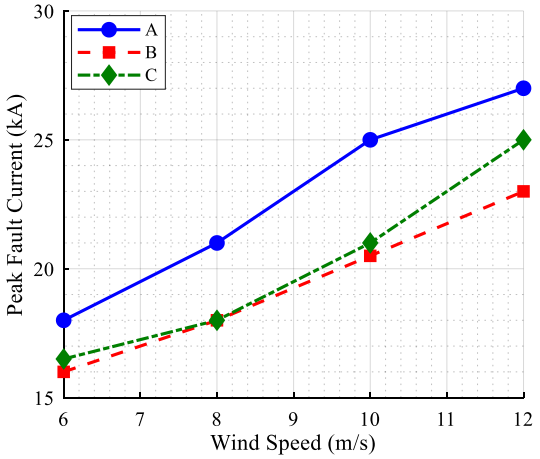

b)

Figure 16. Maximum fault current passes through each phase of the understudied HTS cable under different wind speeds for F1 transient scenario, a) S1, b) S2

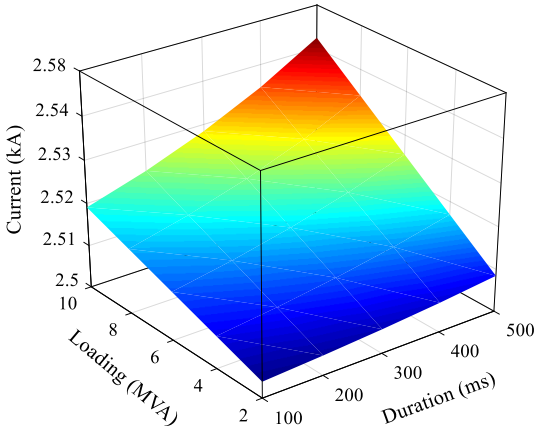

Figure 17. Peak transient current caused by islanding operating mode under different loadings and duration for S1 and IMO2 transient scenario

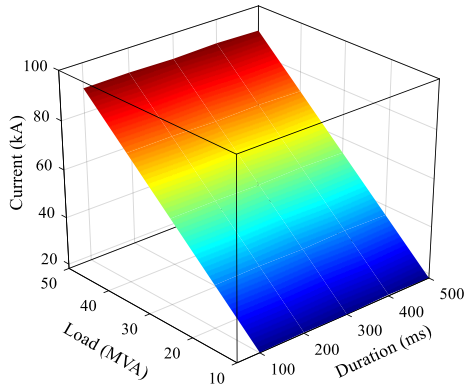

Figure 19. Peak transient current caused by islanding operating mode under different loadings and duration for S2 and IOM2

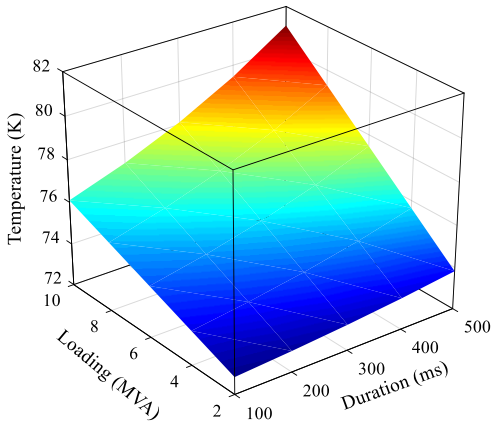

Figure 18. The maximum temperature of the HTS tapes in phase A (as the worst-case scenario) for transient scenario of IOM2 and S1 grid structure

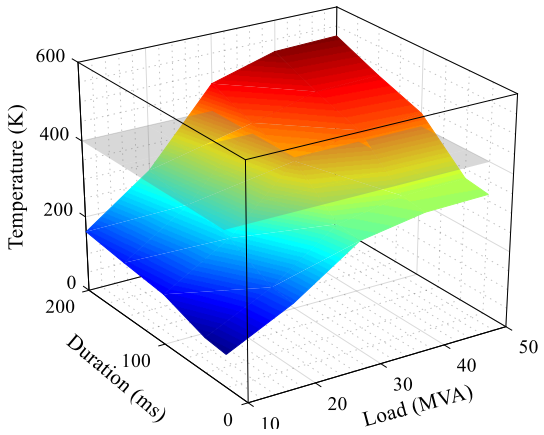

Figure 20. The maximum temperature of the HTS tapes in phase A (as the worst-case scenario) for transient scenario of IOM2 and S2grid structure

This proves the challenges that were expressed earlier in this section. By a slight change in parameters of the grid and fault current reduction, phase C could transit into the flux-flow state rather than the normal state which could lead to burn-out of HTS tapes. Under faulty conditions, it is necessary to analyse the wind speed and transmitted power of the turbine. Due to the fact that wind speed is effective on the performance of the HTS cable, cutting off the turbine when the speed is lower than the nominal speed is highly probable under transient conditions.

C. The islanding operating mode

IOM is a common event for the power systems in which load is supplied by the distributed generations. Under such circumstances, the electrical unbalance between load and generation power injects a current to the HTS cable with a higher amplitude than the nominal current. Islanding mode could occur under different loadings and time duration which impacts the electrothermal behaviour of the HTS cable.

Fig. 17 illustrates the maximum current of the cable during the islanding mode of the grid for different loadings and durations under S1 structure and IOM1 and IOM2. As can be seen, the maximum transient current is about 0.5 kA, 33.3% overcurrent, higher than the nominal current of the HTS cable.

This results in a weak increase in the temperature of HTS tape, as shown in Fig. 18. Under such circumstances, the temperature increases between 2.85% to 17.14% of the base temperature. If the loading exceeds the generated power by the wind farm, islanding mode would impose massive current around 80 kA into the HTS cable. This massive current has a much higher frequency than nominal frequency and would be damped very fast. By varying the load from 10 to 50 MVA in 5 MVA steps, and also increasing the duration of islanding operating mode from 100 to 500 ms, the maximum islanding current varies which is shown in Fig. 19. By imposing these currents to the cable, the temperature varies from 190 K to 600 K, according to Fig. 20. The grey plane shown in Fig. 20, is the maximum tolerable temperature for YBCO tapes. Any temperature increases higher than this plane, causes serious damage and certain burnout of these tapes. According to Fig. 21, for any loading and islanding operation for 50 to 100 ms, the cable would not be in thermal runaway zone while if the islanding operation lasts more than 100 ms and less than 500 ms, for loading more than 20 MVA, the HTS cable would be burnt. At last, any loading for islanding which lasts more than 500 ms, causes the direct burn out of the cable.

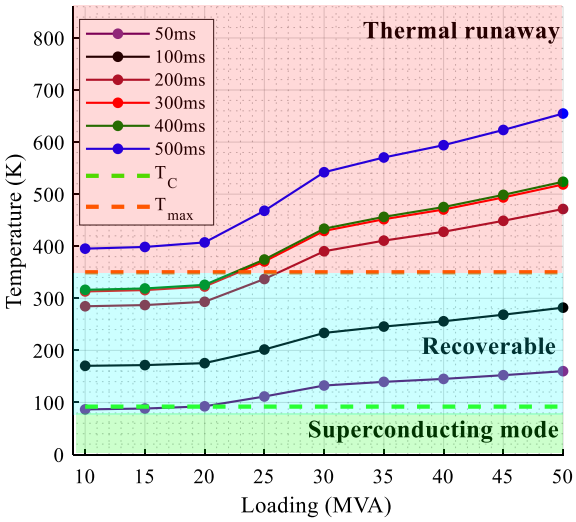

Figure 21. Three possible thermal states after the islanding mode for the second scenario of the grid with respect to IOM2 transient

IV. CONCLUSION

High Temperature Superconducting (HTS) cables are candidates for transmitting the generated power of offshore wind farms to the load centres through power network. They have much lower loss and weight in comparison to conventional transmission lines. However, there is a need for a complete electrothermal analysis, before implementing them in wind farm integrated power systems. This paper has used an equivalent circuit model to characterise the transient-state behaviours of a 3 km long 22.9 kV HTS cable. An electromagnetic coupled with the thermal model is considered. The following results were found for transient mode:

- By a 1 m/s increase in wind speed, the maximum temperature of the cable increases by 21.9%
- The higher wind speed causes a faster transition to non-superconducting state of HTS tapes
- Location of fault is another vital factor affecting the maximum transient current level for both scenarios of the grid
- Under both islanding operating modes for S1 scenario, the occurrence of thermal runaway in superconducting layer is highly possible
- Any islanding operation with a duration higher than 300 ms and loading more than 30 MVA causes the burnout of the superconducting tapes in the S2 scenario
- In islanding mode, for the S1 scenario cable remains in superconducting state while in the S2 scenario, thermal runaway is highly possible.

REFERENCES

[1] H. Díaz and C. G. Soares, "Review of the current status, technology and future trends of offshore wind farms," *Ocean Eng.*, vol. 209, no. 107381, 2020.

[2] R. Cowell, G. Bristow, and M. Munday, "Acceptance, acceptability and environmental justice: the role of community benefits in wind energy development," *J. Environ. Plan. Manag.*, vol. 54, no. 4, pp. 311–324, 2011.

[3] M. Yazdani-Asrami, S. M. Seyyedbarzegar, A. Sadeghi, W. T. B. de Sousa, and D. Kottonau, "High Temperature Superconducting Cables and their Performance against Short Circuit Faults: Current Development, Challenges, Solutions, and Future Trends," *Supercond. Sci. Technol.*, vol. 35, no. 8, p. 083002, 2022.

[4] M. Yazdani-Asrami, A. Sadeghi, S. M. Seyyedbarzegar, and A. Saadat, "Advanced experimental-based data-driven model for the electromechanical behavior of twisted YBCO tapes considering thermomagnetic constraints," *Supercond. Sci. Technol.*, vol. 35, no. 5, p. 054004, 2022, doi: https://doi.org/10.1088/1361-6668/ac57be.

[5] M. Yazdani-Asrami, S. M. Seyyedbarzegar, M. Zhang, and W. Yuan, "Insulation Materials and Systems for Superconducting Powertrain Devices in Future Cryo-Electrified Aircraft: Part I—Material Challenges and Specifications, and Device-Level Application," *IEEE Electr. Insul. Mag.*, vol. 38, no. 2, pp. 23–36, 2022.

[6] M. Yazdani-Asrami *et al.*, "Fault current limiting HTS transformer with extended fault withstand time," *Supercond. Sci. Technol.*, vol. 32, no. 3, 2019, doi: 10.1088/1361-6668/aaf7a8.

[7] H. Daoyu, L. Zhuyong, H. Zhiyong, and J. Zhijian, "Development of a single-phase 330kVA HTS transformer using GdBCO tapes," *Phys. C Supercond. its Appl.*, vol. 539, pp. 8–12, 2017.

[8] W. Song *et al.*, "AC Losses in Noninductive SFCL Solenoidal Coils Wound by Parallel Conductors," *IEEE Trans. Appl. Supercond.*, vol. 30, no. 8, 2020, doi: 10.1109/TASC.2020.3021339.

[9] W. Song *et al.*, "Experimental and Simulation Study of Resistive Helical HTS Fault Current Limiters: Quench and Recovery Characteristics," *IEEE Trans. Appl. Supercond.*, vol. 31, no. 5, 2021, doi: 10.1109/TASC.2021.3061958.

[10] R. A. de Oliveira *et al.*, "Optimized Shape of Short-Circuited HTS Coils by Cutting Process for Superconducting Fault Current Limiters," *IEEE Trans. Appl. Supercond.*, vol. 31, no. 9, pp. 1–9, 2021.

[11] M. Yazdani-Asrami, M. Zhang, and W. Yuan, "Challenges for developing high temperature superconducting ring magnets for rotating electric machine applications in future electric aircrafts," *J. Magn. Magn. Mater.*, vol. 522, p. 167543, 2021, doi: 10.1016/j.jmmm.2020.167543.

[12] K. S. Haran *et al.*, "High power density superconducting rotating machines - Development status and technology roadmap," *Supercond. Sci. Technol.*, vol. 30, no. 12, p. 123002, 2017, doi: 10.1088/1361-6668/aa833e.

[13] A. Morandi, "HTS dc transmission and distribution: Concepts, applications and benefits," *Supercond. Sci. Technol.*, vol. 28, no. 12, p. 123001, 2015, doi: 10.1088/0953-2048/28/12/123001.

[14] D. I. Doukas, "Superconducting Transmission Systems: Review, Classification, and Technology Readiness Assessment," *IEEE Trans. Appl. Supercond.*, vol. 29, no. 5, pp. 1–5, 2019, doi: 10.1109/TASC.2019.2895395.

[15] D. T. Eleni Tsotsopoulou, Xenofon Karagiannis, Panagiotis Papadopoulos, Adam Dyśko, Mohammad Yazdani-Asrami, Campbell Booth, "Time-domain protection of superconducting cables based on artificial intelligence classifiers," *IEEE Access*, vol. 10, pp. 10124–10138, 2022, doi: https://doi.org/10.1109/ACCESS.2022.3142534.

[16] O. Rahman, K. M. Muttaqi, and D. Sutanto, "High temperature superconducting devices and renewable energy resources in future power grids: A case study," *IEEE Trans. Appl. Supercond.*, vol. 29, no. 2, p. 3800404, 2019.

[17] T. T. Nguyen, H.-M. Kim, and H. S. Yang, "Impacts of a LVRT Control Strategy of Offshore Wind Farms on the HTS Power Cable," *Energies*, vol. 13, no. 5, p. 1194, 2020.

[18] J. X. Jin, X. Y. Chen, R. Qu, H. Y. Fang, and Y. Xin, "An integrated low-voltage rated HTS DC power system with multifunctions to suit smart grids," *Phys. C Supercond. its Appl.*, vol. 510, pp. 48–53, 2015, doi: 10.1016/j.physc.2015.01.006.

[19] W. Xiang *et al.*, "DC Fault Study of a Point-to-Point HVDC System Integrating Offshore Wind Farm using High-Temperature Superconductor DC Cables," *IEEE Trans. Energy Convers.*, vol. 8969, no. c, pp. 1–11, 2021, doi: 10.1109/TEC.2021.3094308.

[20] H. Mohamad, H. Mokhlis, A. H. AbuBakar, and H. W. Ping, "A review on islanding operation and control for distribution network connected with small hydro power plant," *Renew. Sustain. Energy*

Rev., vol. 15, no. 8, pp. 3952–3962, 2011.

[21] R. Brundlinger and B. Bletterie, "Unintentional islanding in distribution grids with a high penetration of inverter-based DG: Probability for islanding and protection methods," in *2005 IEEE Russia Power Tech*, 2005, pp. 1–7.

[22] K. Maki, A. Kulmala, S. Repo, and P. Jarventausta, "Problems related to Islanding Protection of Distributed Generation in Distribution Network," in *2007 IEEE Lausanne Power Tech*, 2007, pp. 467–472.

[23] F. Katiraei, M. R. Iravani, and P. W. Lehn, "Micro-grid autonomous operation during and subsequent to islanding process," *IEEE Trans. Power Deliv.*, vol. 20, no. 1, pp. 248–257, 2005.

[24] N. Shafique, S. Raza, H. M. Munir, S. S. H. Bukhari, and J.-S. Ro, "Islanding Detection Strategy for Wind Farm Based on Performance Analysis of Passive Indices Having Negligible NDZ," *Appl. Sci.*, vol. 11, no. 21, p. 9989, 2021.

[25] C. Lee, J. Choi, H. Yang, M. Park, and M. Iwakuma, "Economic evaluation of 23 kV tri-axial HTS cable application to power system," *IEEE Trans. Appl. Supercond.*, vol. 29, no. 5, pp. 5–11, 2019, doi: 10.1109/TASC.2019.2908608.

[26] T. Nguyen *et al.*, "A simplified model of coaxial, multilayer high-temperature superconducting power cables with Cu formers for transient studies," *Energies*, vol. 12, no. 8, p. 1514, 2019.

[27] A. Sadeghi, S. M. Seyyed Barzegar, and M. Yazdani-Asrami, "A Simple and Fast Computation Equivalent Circuit Model to Investigate the Effect of Tape Twisting on the AC Loss of HTS Cables," *Eng. Technol. Appl. Sci. Res.*, vol. 12, no. 1, pp. 8168–8174, Feb. 2022, doi: 10.48084/etasr.4382.

[28] Y. Lei, A. Mullane, G. Lightbody, and R. Yacamini, "Modeling of the wind turbine with a doubly fed induction generator for grid integration studies," *IEEE Trans. Energy Convers.*, vol. 21, no. 1, pp. 257–264, 2006.

[29] L. Fan, R. Kavasseri, Z. L. Miao, and C. Zhu, "Modeling of DFIG-based wind farms for SSR analysis," *IEEE Trans. Power Deliv.*, vol. 25, no. 4, pp. 2073–2082, 2010.

[30] A. Sadeghi, S. M. Seyyedbarzegar, and M. Yazdani-Asrami, "Transient analysis of a 22.9 kV/2 kA HTS cable under short circuit using equivalent circuit model considering different fault parameters," *Phys. C Supercond. its Appl.*, vol. 589, no. July, p. 1353935, 2021, doi: 10.1016/j.physc.2021.1353935.

[31] J. Duron, F. Grilli, L. Antognazza, M. Decroux, B. Dutoit, and Ø. Fischer, "Finite-element modelling of YBCO fault current limiter with temperature dependent parameters," *Supercond. Sci. Technol.*, vol. 20, no. 4, p. 338, 2007.

[32] M. Yazdani-Asrami, M. Staines, G. Sidorov, and A. Eicher, "Heat transfer and recovery performance enhancement of metal and superconducting tapes under high current pulses for improving fault current-limiting behaviour of HTS transformers," *Supercond. Sci. Technol.*, vol. 33, no. 9, p. 095014, 2020.

[33] U. A. Khan, J. K. Seong, S. H. Lee, S. H. Lim, and B. W. Lee, "Feasibility analysis of the positioning of superconducting fault current limiters for the smart grid application using simulink and simpowersystem," *IEEE Trans. Appl. Supercond.*, vol. 21, no. 3, pp. 2165–2169, 2011.

[34] Y. Zhao, T. K. Saha, O. Krause, and Y. Li, "Performance analysis of resistive and flux-lock type SFCL in electricity networks with DGs," in *2015 IEEE Power & Energy Society General Meeting*, 2015, pp. 1–5.